

ACSC: Automatic Calibration for Non-repetitive Scanning Solid-State LiDAR and Camera Systems

Jiahe Cui¹²³, Jianwei Niu¹²³, Zhenchao Ouyang^{*3}, Yunxiang He³ and Dian Liu³

Abstract—Recently, the rapid development of Solid-State LiDAR (SSL) enables low-cost and efficient obtainment of 3D point clouds from the environment, which has inspired a large quantity of studies and applications. However, the non-uniformity of its scanning pattern, and the inconsistency of the ranging error distribution bring challenges to its calibration task. In this paper, we proposed a fully automatic calibration method for the non-repetitive scanning SSL and camera systems. First, a temporal-spatial-based geometric feature refinement method is presented, to extract effective features from SSL point clouds; then, the 3D corners of the calibration target (a printed checkerboard) are estimated with the reflectance distribution of points. Based on the above, a target-based extrinsic calibration method is finally proposed. We evaluate the proposed method on different types of LiDAR and camera sensor combinations in real conditions, and achieve accuracy and robustness calibration results. The code is available at <https://github.com/HViktorTsoi/ACSC.git>.

I. INTRODUCTION

Multi-sensor fusion has always been essential to robotics and self-driving systems, for accurate perception of the surrounding environment. Among different types of fusion, the commonest one is the combination of LiDAR (Light Detection And Ranging) and the optical camera, especially in the tasks of vision-based odometry and mapping [1], object detection and tracking tasks [2]–[5]. In fusing the multi-modal data from LiDAR-camera systems, the first and most critical step is the accurate extrinsic calibration. The general calibration process is to detect the multiple corresponding 3D-2D corners, and then solve the relative pose between LiDAR and the camera by utilizing the PnP (Perspective-N-Point) method. Thus, it is essential to find the corresponding features accurately by geometric and texture constraints from point clouds and images.

In the past two years, the Solid-State LiDAR (SSL) system has begun to be widely adopted by different intelligent unmanned platforms [6]–[8], due to its low price, automotive-grade design, and similar ranging performance as high-definition LiDARs. However, The characteristic of SSL brings new challenges to sensor deployment, especially for the sensor calibration process: because the non-repetitive scanning mode is utilized by this LiDAR model, the spatial distribution of points is nonuniform; its ranging measurement is sensitive to the texture and color of targets; and its

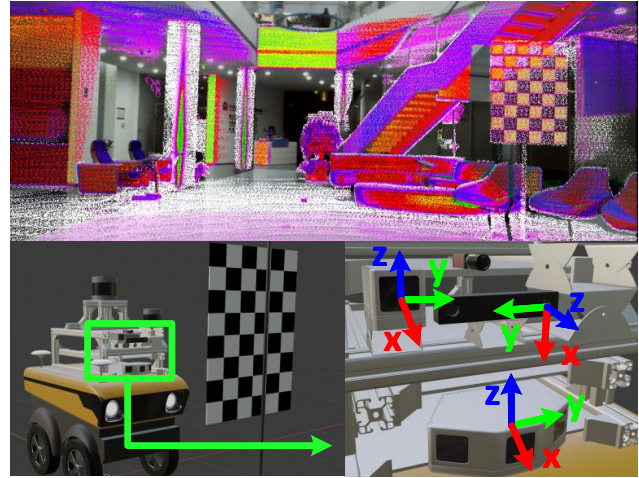


Fig. 1: (a) Top: The reprojection of integrated point clouds to the image using the extrinsic parameter solved by ACSC; (b) Bottom: The calibration target we use is a printed checkerboard; the placement is shown in the left; the sensor setup and its coordinate system are described in the right.

ranging error is also non-uniformly distributed due to its low-cost measuring unit. Such drawbacks seriously affected corresponding feature extraction in point clouds, and thus reduce the performance of automatic calibration. There are few former studies on automatic calibration of SSL-camera systems.

To solve the above-mentioned problems, this paper proposes ACSC, an Automatic extrinsic Calibration method for the SSL-Camera systems. We first design a time-domain integration and point cloud feature refinement pipeline to extract as much effective information as possible for non-repetitive scanning point clouds, and proposed a 3D corner extraction method by utilizing the reflectance intensity distribution of the calibration target. Based on the 3D corners and corresponding 2D corners (from the optical image), a target-based calibration method is proposed. We also evaluated the proposed method in different types of SSL, e.g., the Livox Mid-100/40 and Horizon SSL, and camera combinations. The main contributions of this paper are summarized as follows:

- An automatic target-based calibration method for the SSL and camera system is proposed;
- A temporal-spatial-based geometric feature refinement, and reflectance intensity distribution-based 3D corner estimation pipeline for point clouds from non-repetitive scanning SSL is presented;

*Email: ouyangkid@buaa.edu.cn

¹State Key Laboratory of Virtual Reality Technology and Systems, Beihang University, Beijing 100191, China

²Beijing Advanced Innovation Center for Big Data and Brain Computing (BDBC), Beihang University, Beijing 100191, China

³Hangzhou Innovation Institution, Beihang University, Hangzhou 310000, Zhejiang, China

- To evaluate the calibration performance, multiple real-world experiments based on various combinations of LiDARs with cameras are deployed, and the proposed method can successfully solve extrinsic parameters from various types of LiDAR-camera systems.

II. RELATED WORKS

Most of the extrinsic calibration methods are based on reference targets, the common idea is to design calibration targets or corresponding features that can be clearly detected in all sensor FOVs. The planar board is the most commonly used calibration target for both intrinsic and extrinsic calibrations of the monocular/stereo cameras [9]–[12]. Fremont et al. [13] designed a black circle-based planar board, then searched the 3D coordinates of the circle center and the normal vector of the plane for extrinsic calibration between a camera and a LiDAR. Zhou et al. [14] proposed a single-shot calibration method, by extracting line features from the LiDAR points and the image. Wang et al. [15] proposed a 3D corner estimation algorithm based on the correlation between the reflectance intensity of the laser and the color of the calibration target.

The targetless-based method tries to find natural patterns (mainly the line or orthogonal) from the scene, and formulates them in terms of geometric constraints to then solve the extrinsic. Basically, they can be divided into static-based and motion-based methods. The former one is similar to target-based registration, finding reference features with static targets. Scaramuzza et al. [16] proposed an extrinsic calibration technique that requires manually associating 2D points on the image with 3D points on the point cloud. In [17], the trihedral features detected from the environment, such as walls and corners on the street, are used for calibration, however, the method relies on high-cost Velodyne-64E to find the trihedron patterns. [18] proposed a targetless calibration method, the extrinsic parameter is solved by maximizing the mutual information (MI) obtained between the sensor-measured surface intensities from images or point clouds. In contrast, motion-based methods [19] use Simultaneous Localization And Mapping (SLAM) technologies, the extrinsic is calculated based on the motion estimation between the fixed sensors, by minimizing the trajectory to trajectory matching error.

The methods above have achieved fine results on mechanical LiDAR and camera systems, but it is challenging to generalize them to SSL, whose point cloud measurement have significantly different feature distribution from the mechanical models. Scaramuzza et al. [20] proposed a geometric model-based method for SSL intrinsic correction. Liu et al. [21] proposed a multi-SSL calibration method by utilizing LOAM-based trajectory matching. The intensity value is related to the superficial texture and color of the measured targets; therefore, it can provide as much plentiful semantic information as optical images, especially for dense point cloud from non-repetitive scanning SSL after time-domain stacking. In this paper, by utilizing temporal integration and feature refinement, the proposed calibration

method can make the best of the non-repetitive pattern of SSL, and achieve accuracy calibration results.

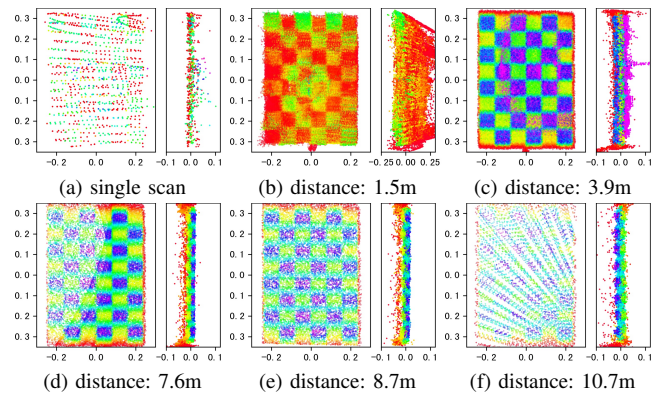


Fig. 2: The integrated (without feature refinement) checkerboard point clouds from non-repeat scanning SSL (left: front view; right: side view).

III. METHOD

For the SSL-camera system, the problem of extrinsic calibration is to estimate the relative rotation and translation between the two sensors, namely, the task is to solve the extrinsic parameter matrix ($E \in SE3$) based on the corresponding 3D-2D corners extracted from same frame of the two different sensors, respectively. The proposed method uses a printed checkerboard as the calibration target, the dimension of the inner corners on the board is $N_h \times N_w$, and the inner grid size is G_s .

However, the main challenge is how to accurately extract the corners from the unstably-distributed point clouds. We conduct research on the representative Livox series LiDAR in this paper, and Fig. 2 shows several typical patterns obtained in scanning of the calibration target: 1) The non-repetitive scanning pattern causes sparse single frame measurement. Although the point cloud can be densified by multiple-frame stacking, the outliers are also reserved (Fig. 2 (a)-(f)). 2) The range measurement has large variance in axial direction (direction of beams). The closer the distance, the more serious the jitter (side views in Fig. 2). 3) The special scanning pattern also leads to uneven distribution of scan lines (Fig. 2 (d), (e) and (f)). The proposed calibration method considers the above characteristics, and thus can accurately extract corresponding feature from SSL and camera. The whole workflow is illustrated in Fig. 3.

A. Calibration Target Feature Refinement

1) *Time-domain integration of point clouds*: We take advantage of the non-repetitive scanning pattern, and integrate the continuous scans in the time domain to densify the point clouds, instead of using single scan Fig. 2 (a) directly. In this way, the dense checkerboard measurement can be obtained, with intensity features that provides as much semantic information as the image does. However, if incoming point clouds are simply stacked, the noise points from each frame will also be accumulated, and eventually cause fuzzy results (as shown in Fig. 2); therefore, we first

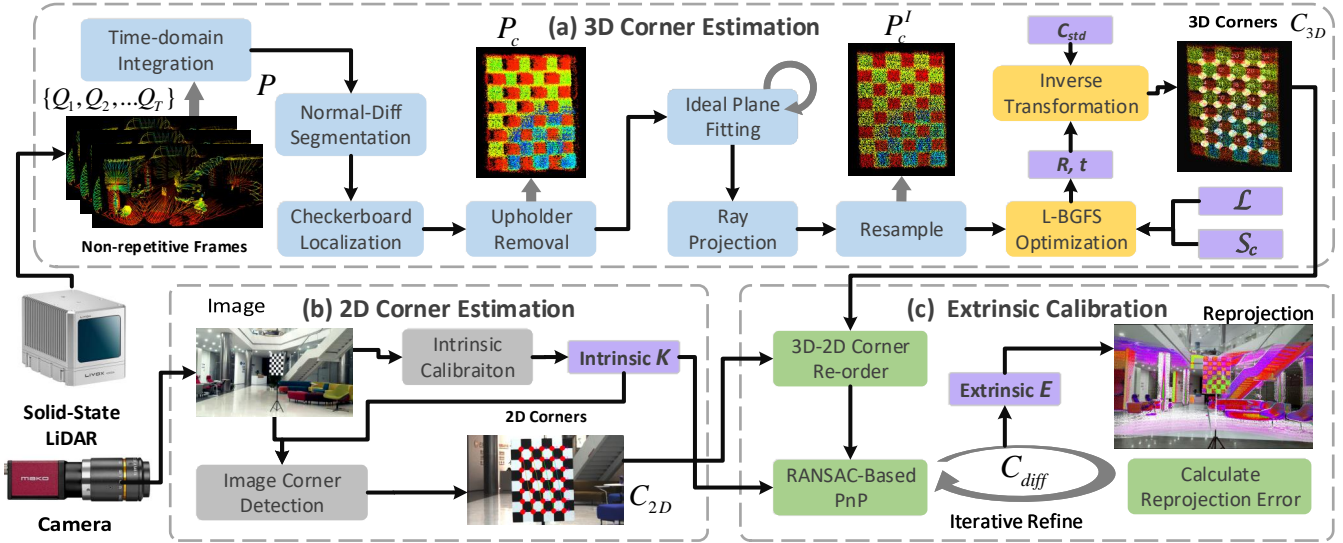


Fig. 3: The proposed calibration method. (a) The feature refinement and checkerboard inner corner estimation process of point clouds from SSL. The input $\{Q_1, Q_2, \dots, Q_T\}$ are incoming frames of SSL, S_c represents the standard model constructed from the geometric parameter of the calibration target we use, C_{std} is the corner generated from S_c , and \mathcal{L} is the similarity measurement function for optimizing the 3D corner location; (b) 2D corner estimation from images; (c) The extrinsic calibration process.

utilized statistical outliers removal for every incoming frame, based on the neighbor density distribution of points, the integrate the noise-free points in time-domain, the detailed process is shown in Algorithm. 1.

After integration, the surface normal of the points is distributed more continuously than that of a single scan, therefore, the normal difference-based segmentation [22] is first deployed to extract the candidate clusters that may contains the checkerboard. We then sort the clusters by the standard target similarity measurement \mathcal{L} (presented in Section III-B), to measure the difference between the cluster and the calibration target, and only the clusters with the minimum difference are maintained, as the located checkerboard measurement (marked as P_c).

2) *Feature refinement*: To obtain a noised-free and accurate checkerboard measurement, a series of point cloud feature enhancement methods are designed, and the whole process is shown in Fig. 4.

Considering the upholder/ground points may be connected to the checkerboard P_c after being segmented from the background, we first remove these points. Suppose the placement of the sensor and the checkerboard are as shown in Fig. 1, only the upper and lower boundaries of the checkerboard points in the Z-axis direction are needed to be determined. For the upper boundary, we choose the Z coordinate of the highest point $Z_{top} = \max P_c^z$. The lower boundary is calculated based on both the width distribution H of checkerboard points along Z-axis, and the checkerboard size constraint:

$$Z_{down} = \arg \max_z \frac{\partial H(\|P_c^{xy} - \frac{1}{N} \sum P_c^{xy}\|, z)}{\partial z} + w \frac{|(Z_{top} - z) - N_h G_s|}{N_h G_s} \quad (1)$$

Algorithm 1: The time-domain integration process of incoming point cloud frames from SSL.

Input :

T frames of point cloud
 $Q = \{Q_1, Q_2, \dots, Q_T\}$;
 Threshold of neighbor size K ;
 Scaling factor $scale_{std}$;

Output:

Stacked point cloud P ;

```

1 Initialize  $P = \emptyset$ ;
2 repeat
3   for frame  $Q_t$ , build KD-Tree;
4   for each point  $q_i \in Q_t$  do
5     search the  $K$  nearest points of  $q_i$ ;
6     calculate the average distance ( $disK_i$ ) of
       the  $K$  neighbours;
7   end
8   calculate the mean distance  $meanK$  and
       standard deviation  $stdK$  of
       [ $disK_0, disK_1, \dots, disK_N$ ];
9    $thresh = meanK + scale_{std} \times stdK$ ;
10  for each point  $q_i \in Q_t$  do
11    if  $disK_i < thresh$  then
12      Remove  $q_i$  from  $Q_t$ ;
13  end
14   $P = P + \{Q_t\}$ ;
15 until
    All  $T$  frames of point clouds in  $Q$  are consumed;

```

Where w is the ratio of checkerboard size constraint. All the other points that are not in this range (Z_{down}, Z_{top}) will be removed. For simplicity, the remained checkerboard point

cloud is also marked as P_c .

As shown in Fig. 2, the point clouds are scattered along the axial direction due to due systematic error of SSL measurement, while in the ideal situation, all points are supposed to fall on the checkerboard plane, therefore, it is hard to estimate the accurate corner coordinates. We thus designed an iteratively refining method to fit the point cloud to the ideal plane where the checkerboard lies. During each iteration, we first use the RANSAC-based method to fit the optimal plane. The point clouds P'_c within a distance of σ to the plane are reserved:

$$P'_c = \{(x_0, y_0, z_0) \in P_c \mid \frac{|Ax_0 + By_0 + Cz_0 + D|}{\sqrt{A^2 + B^2 + C^2}} < \sigma\} \quad (2)$$

Here, the A , B , C and D are the estimated parameter of the fitted plane. Now the point set P'_c is closer to the ideal plane than P_c , we then shrink σ and repeat the fitting and filtering process. When all the point clouds are within the threshold of the current iteration, the calculation stops. According to the ranging principle of SSL, the ranging measurement of a laser beam may contain error in the radial direction (from the obstacle to the sensor center), while that at the azimuth or polar directions can be ignored. Based on this prior, the projective transformation model are then utilized for projecting the noise point cloud onto the ideal plane, as described in Eq. 3.

$$P_c^I = \{(x_0t, y_0t, z_0t) \mid (x_0, y_0, z_0) \in P'_c\} \quad (3)$$

where

$$t = -D/(Ax_0 + By_0 + Cz_0) \quad (4)$$

Afterwards, to reduce the influence of non-uniformity caused by the non-repetitive scanning pattern (as shown in Fig. 2 (d) and (f)), we divide the unified points P_c^I is into multiple grids, and then adopt random sampling to each grid, to maintain the point cloud density not greater than δ_ρ . By combining the downsampled grid together, we can get a checkerboard point cloud with uniform density. This operation can reduce the impact of high-density areas on penalty function during later corner fitting, and lead to better overall corner detection results.

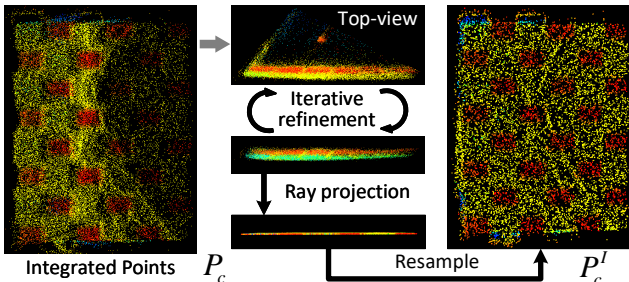


Fig. 4: The feature refinement process, from raw point cloud of the checkerboard P_c , which is segmented from background points, to the noise-free measurement P_c^I .

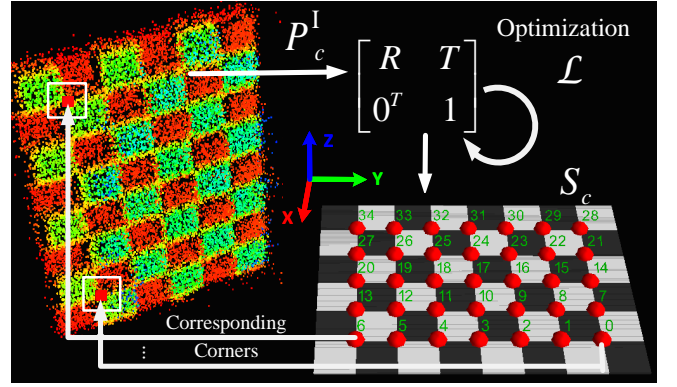


Fig. 5: Schematic diagram of corner estimation. The transformation from the refined checkerboard measurement P_c^I to the standard model S_c is first solved using the reflectance distribution, and then used to inversely transform the corners of the S_c to original checkerboard.

B. 3D Corner Estimation

We introduce a non-linear optimization method, that is constrained by the global reflectance distribution of checkerboard measurement, for estimating the corners, the schematic diagram is shown in Fig. 5. Given the geometrical parameter of the checkerboard $\{N_w, N_h, G_s\}$, a standard checkerboard model S_c with reflectance information can be constructed as Eq.5:

$$S_c = \{(x, y, z, I) \mid x \in (0, N_w G_s), y \in (0, N_h G_s), z = 0, I = \delta(x, y, z)\} \quad (5)$$

Here, δ is a binary function that indicates the pattern of checkerboard at (x, y, z) . Considering the measured value of the checkerboard point cloud (P_c^I) by LiDAR is physically the same size with S_c without scaling, the checkerboard measurement and the standard model can be aligned through rigid body transformation, and the 3D inner corner coordinates can also be solved by inverse transformation, since the corners of the standard model are already known from geometrical parameters. Therefore, we convert the 3D corner estimation into a non-linear optimization problem: solving the transformation parameters $\{R, t\}$ that make the measured value of the transformed checkerboard point cloud closest to the ideal standard model.

The critical step is designing the similarity function, that can accurately evaluate the pose-difference between the measured value P_c^I and the standard model S_c . We found that, as shown in Fig. 6, the reflectance of the checkerboard measurement P_c and the black-white pattern on the physical checkerboard basically shows the same spatial distribution, therefore, we formulates the similarity as the reflectance distribution difference, defined as Eq. 6:

$$\begin{aligned} \mathcal{L}(S_c^{xyz}, \tilde{P}_c^{xyz}, I_S, I_P | R, t) &= \sum_{\tilde{p}_i \in \tilde{P}_c}^{N_c} \mathcal{L}_1 + \mathcal{L}_2, \\ \mathcal{L}_1 &= \delta_{in}(\tilde{p}_i, S_c^{xyz}) | I_S(\tilde{p}_i) - I_P(\tilde{p}_i) | d(\tilde{p}_i, G_i), \\ \mathcal{L}_2 &= (1 - \delta_{in}(\tilde{p}_i, S_c^{xyz})) d(\tilde{p}_i, G_i) \end{aligned} \quad (6)$$

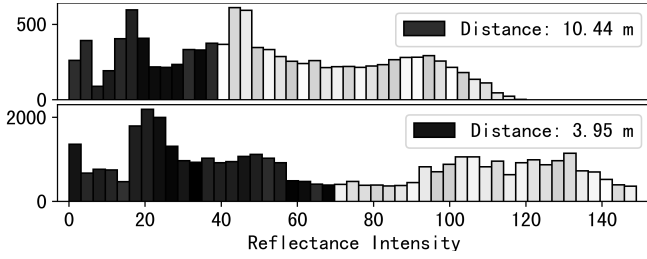


Fig. 6: Reflectivity distribution of checkerboard point cloud under different distances. The black and white bars respectively represent the reflectivity of the corresponding color grid in the checkerboard.

Here, \tilde{P}_c^{xyz} is the transformed geometry coordinates of the checkerboard points:

$$\tilde{P}_c^{xyz} = \begin{bmatrix} R & t \\ 0^T & 1 \end{bmatrix} P_c^{xyz}, R \in SO3, t \in R^3 \quad (7)$$

I_P is the corresponding reflectance intensity value, S_c^{xyz} and I_S are the same representation for the standard model; N_c is the number of points on the checkerboard; δ_{in} is the discriminant function for judging whether the point \tilde{p}_i falls within the border rectangle of the standard checkerboard, and G_i is the closet corner to \tilde{p}_i , as defined in Eq. 8:

$$G_i = \arg \min_{G_j} |\tilde{p}_i - G_j|, \quad (8)$$

$$d(\tilde{p}_i, G_i) = |G_i^x - \tilde{p}_i^x| + |G_i^y - \tilde{p}_i^y|$$

Thus, the optimal solution of R, t can be solved through nonlinear optimization, the L-BGFS [23] method is utilized for optimizing this problem. Combined with corners C_{std} that are directly generated by the geometric parameter of the checkerboard, the final estimated corner coordinates C_{3D} of the point cloud (Eq. 9) can be obtained through inverse transformation:

$$C_{3D} = \begin{bmatrix} R^T & -R^T t \\ 0^T & 1 \end{bmatrix} C_{std}. \quad (9)$$

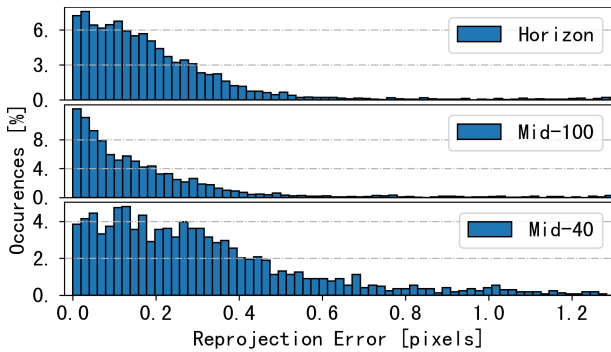


Fig. 8: Normalized reprojection error to evaluate performance of extrinsic calibration of different SSL models.

C. Extrinsic Calibration

2D corner detection from image. The checkerboard corner detection algorithm [24] is used to detect the corners C_{2D} from the image, which is corresponding to integrated point cloud frame from SSL. Note that due to the symmetry

of the checkerboard along the diagonal direction, the order of the corner points detected in the image and in the point cloud may be ambiguous. We reorder the detected corner points and index them from the lower left corner.

Iteratively extrinsic parameter solving. Considering that the limited samples of checkerboard measurement, for the obtained 3D-2D corners, the RANSCA-based PnP is first adopted to get a initial extrinsic solution E_0 ; then, the corners with high reprojection error (calculated based on E_0) are dropped, and the PnP-solving and reprojection evaluating process continues repeatedly, until all errors are lower than δ_{reproj} . Then final extrinsic matrix is denoted as E .

IV. EXPERIMENTS AND RESULTS

A. Calibration Setup

In real-condition calibration process, the SSL and camera are required to be in a fixed relative position, and the intrinsic of camera are assumed to be known. Through multiple sampling of the checkerboard placed in different positions and orientations within the FOV of the sensors, the corresponding images and multi-frame point cloud are collected, and are then used to calculate the extrinsic parameters.

We evaluate the proposed method on multiple representative SSL and camera models, the sensor details are described in Table. I.

Sensor type	Sensor model	FOV($^\circ$)	
		H	V
Solid-state LiDAR	Livox Horizon	81.7	25.1
	Livox Mid-40	38.4	38.4
	Livox Mid-100	98.4	38.4
Camera	MYNT EYE-D D1000	103.0	55.0
	PointGrey Flea3	111.0	82.9

TABLE I: The detailed model and parameter of sensors we used to evaluate the proposed calibration method.

B. Reprojection Visualization

To visualize the calibration results, we project the point cloud (collected from both indoor and outdoor environments) onto the image plane with the solved extrinsic parameter matrix, as shown in Fig. 7 (a)-(b), with the colors of the projected points generated according to the corresponding reflectivity. For clarity, the contour is extracted on the image to make the matching difference in the projection results more significant in Fig. 7 (b). It can be seen (especially from the partial enlarged view) that the projected points (with different reflectivity) matches the original image precisely. Fig. 7 (c) shows an example of projecting the 2D image pixels back into the 3D space (also called point cloud colorization [25]), it can be seen that the projected image texture is also accurately matched to the 3D point cloud.

C. Normalized Reprojection Error

In real conditions, it is hard to get a reference ground-truth measurement of the extrinsic parameters between LiDAR and

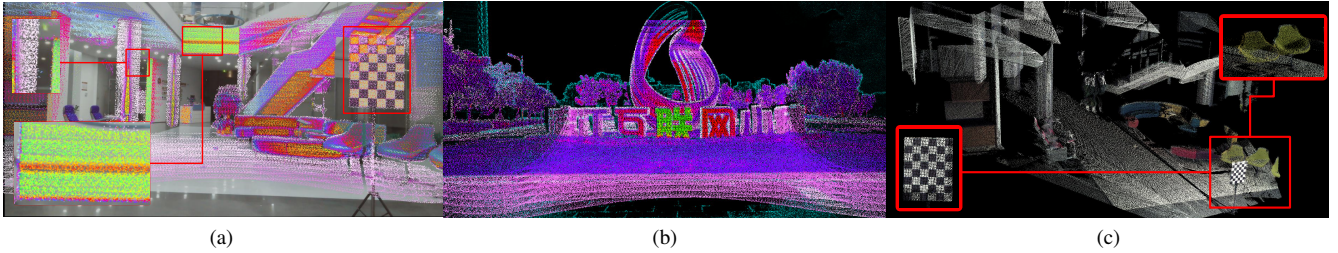


Fig. 7: (a) Visualization of the calibration results. The point clouds are projected onto the image plane based on the solved extrinsic parameter matrix; (b) The projected point clouds on images (with the edge enhanced) in outdoor environment; (c) The colorized point clouds by projecting the pixel from the image using the calibration result.

camera. A compromise solution is to evaluate the result by measuring the errors between the reprojected checkerboard corners from the point cloud and from the image [26]. We first project the estimated 3D corners of checkerboard C_{3D} to 2D space, based on the camera intrinsic K and estimated extrinsic E . Then, the corners from image C_{2D} are treated as pseudo ground-truth to calculate reprojection error. Notice that, due to the perspective projection of camera, the distance of the checkerboard placements may affect the scales of reprojected points (for instance, at the placements that are too far, the reprojection error is smaller than the actual value), therefore, we re-scale the reprojection by distance normalization to reduce this bias, as described in Eq. 10:

$$NRE = \sum_{p \in C'_{3D}, c_{2d} \in C_{2D}} \frac{d(p)}{d_{max}} (|p - c_{2d}|) \quad (10)$$

$$C'_{3D} = \frac{1}{z} EK \begin{bmatrix} C_{3D}^x \\ C_{3D}^y \\ C_{3D}^z \end{bmatrix} \quad (11)$$

Here, c_{2d} is the closest image pixel to the reprojected point p , and $d(p)$ is the distance of p from LiDAR center. Fig. 8 illustrates the normalized reprojection errors of different LiDAR models, it can be seen that most reprojection errors are within 0.6 pixel, which proves the accuracy of the proposed method. For Fig. 8 (c), the reprojection error of Mid-40 is a slightly higher than that of the other two types, this is because it has a smaller sensor FOV (about 40 degree), thus less target placements can be sampled, causing absent constraints when solving PnP problem. As a result, the calculation accuracy of extrinsic parameters decreases.

Method	AVG	$NRE < pe$ (%)			
		$pe = 0.5$	$= 1$	$= 5$	$= 10$
MI [18]	9.77	1.89	3.93	39.34	60.15
ILCC [15]	4.76	5.64	10.60	59.40	90.60
HUANG [12]	7.73	4.54	9.41	39.33	70.59
Ours	2.11	69.33	75.41	87.16	92.75

TABLE II: Quantitative evaluation of the calibration methods. AVG denotes the average normalized reprojection error (pixels); $NRE < pe$ denotes the percentage of corners with reprojection error less than pe pixels.

Table. II shows the quantitative evaluation results of the proposed method and previous studies on the SSL-camera

calibration task. Notice that, due to the heavily dependent on the ring-based scanning pattern of mechanical LiDAR (e.g. Velodyne HDL64), most of the implementations of previous studies([12], [15]) failed to detect the calibration target from SSL point clouds, and therefore refused to calculate extrinsic parameter; only after we resample the integrated points to 128-channel LiDAR-like pattern, can they generate feasible solutions. The proposed method performs more accurate calibration results than the others by a large margin, especially for $pe < 0.5$ and $pe < 1$, due to the consideration of characteristics of SSL.

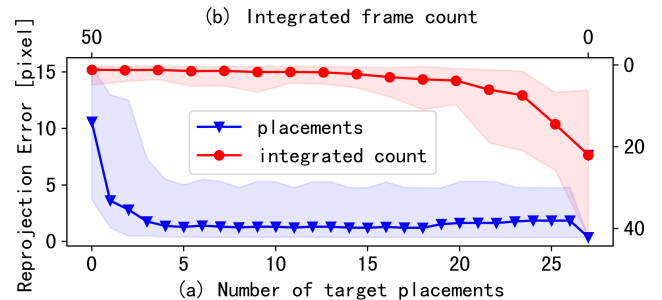


Fig. 9: Impact of different target placements and integrated frame count on the calibration performance.

We also investigate the influencing factors that affect the reprojection error. As show in Fig. 9 (a), the proposed method achieve better performance by adding samples of target placements with different distances and poses, and the error can remain stable with a minimal samples at 5~6 poses. Fig. 9 (b) shows that, increasing the integration time can also improve the calibration performance, which verifies the effect of time-domain integration.

D. Evaluation of 3D Corner Estimation

The performance of the proposed method is highly related to the estimated checkerboard corners. Therefore, we further discuss the performance of corner estimation. Fig. 10 illustrates the distribution of cost function \mathcal{L} and reprojection errors during corner point estimation. The X and Y axes in each subplot donates partial dimensions of the optimization variables (i.e., the transformation between the P_c^I and the standard checkerboard model S_c), the left column is the distribution of similarity function \mathcal{L} , and the right column is that of the reprojection error. It can be seen, that in the space

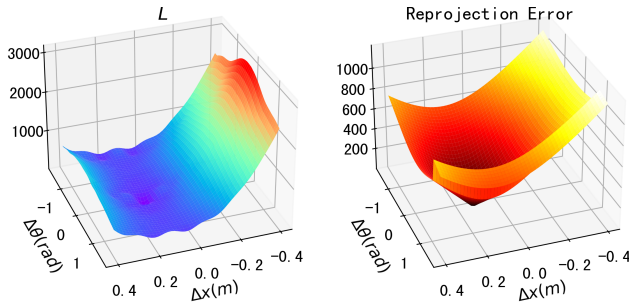


Fig. 10: Distribution of cost function \mathcal{L} and reprojection error with the increments of optimizing variables, i.e. the rigid body transformation parameters between calibration target measurement and standard calibration board model.

which the optimization variables spin, the minimum of \mathcal{L} and the reprojection error are corresponding to the similar region, which means that, as long as a set of optimal solutions for 3D corners are found, the optimal extrinsic parameters can be solved correspondingly. This can prove the rationality of the proposed method from one aspect. Fig. 11 is the visualization result of the checkerboard corner detected from point cloud and image, respectively, it also shows the consistency of estimated corners both from 2D and 3D space. More detailed experiments can be found on our project website (link in the abstract).

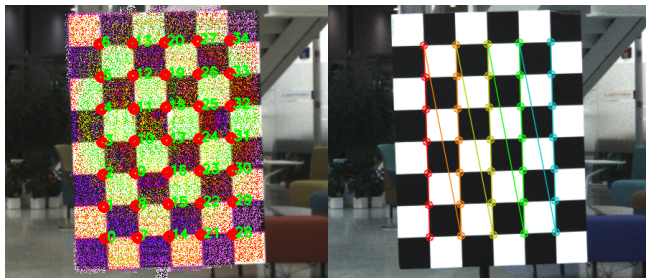


Fig. 11: Visualization the estimated corners of the calibration target. The left is the reprojection of points from SSL, the red dots are reprojection of detected 3D corners; the right is detected 2D corners directly from image.

V. CONCLUSION

This paper proposes a novel extrinsic calibration method for SSL-camera systems. With the proposed time-domain integration and feature refinement pipeline, effective information from fuzzy LiDAR measurement can be extracted; based on the reflectance distribution of calibration target point clouds, we proposed a 3D corner estimation from checkerboard measurement, and combine with the 2D corner extracted from the images, the extrinsic parameters are solved by the proposed calibration method. The whole workflow is fully automated, only needs the user to change the position of the checkerboard several times. The extensive experiments demonstrate that our method can perform accurate calibration in real-world conditions. Future work includes

conducting a more systematic analysis of the calibration process, and expanding the method into dynamic scenarios.

REFERENCES

- [1] César Debeunne and Damien Vivet. A review of visual-lidar fusion based simultaneous localization and mapping. *Sensors*, 20(7):2068, 2020.
- [2] Xiaoyun Dong, Jianwei Niu, Jiahe Cui, Zongkai Fu, and Zhenchao Ouyang. Fast segmentation-based object tracking model for autonomous vehicles. In *International Conference on Algorithms and Architectures for Parallel Processing*, pages 259–273. Springer, 2020.
- [3] Charles R Qi, Xinlei Chen, Or Litany, and Leonidas J Guibas. Imvotenet: Boosting 3d object detection in point clouds with image votes. In *Proceedings of the IEEE/CVF Conference on Computer Vision and Pattern Recognition*, pages 4404–4413, 2020.
- [4] Zhenchao Ouyang, Chunyuan Wang, Yu Liu, and Jianwei Niu. Multiview cnn model for sensor fusion based vehicle detection. In *Pacific Rim Conference on Multimedia*, pages 459–470. Springer, 2018.
- [5] Maximilian Jaritz, Tuan-Hung Vu, Raoul de Charette, Emilie Wirbel, and Patrick Pérez. xmuda: Cross-modal unsupervised domain adaptation for 3d semantic segmentation. In *Proceedings of the IEEE/CVF Conference on Computer Vision and Pattern Recognition*, pages 12605–12614, 2020.
- [6] Jiarong Lin and Fu Zhang. Loam livox: A fast, robust, high-precision lidar odometry and mapping package for lidars of small fov. In *2020 IEEE International Conference on Robotics and Automation (ICRA)*, pages 3126–3131. IEEE, 2020.
- [7] Zheng Liu and Fu Zhang. Balm: Bundle adjustment for lidar mapping. *arXiv preprint arXiv:2010.08215*, 2020.
- [8] Jiarong Lin and Fu Zhang. A fast, complete, point cloud based loop closure for lidar odometry and mapping. *arXiv preprint arXiv:1909.11811*, 2019.
- [9] Peter Fuersattel, Claus Plank, Andreas Maier, and Christian Riess. Accurate laser scanner to camera calibration with application to range sensor evaluation. *IPSN Transactions on Computer Vision and Applications*, 9(1):1–12, 2017.
- [10] Changjun Gu, Yang Cong, and Gan Sun. Environment driven underwater camera-imu calibration for monocular visual-inertial slam. In *2019 International Conference on Robotics and Automation (ICRA)*, pages 2405–2411. IEEE, 2019.
- [11] A Prokos, I Kalisperakis, E Petsa, and G Karras. Automatic calibration of stereo-cameras using ordinary chess-board patterns. *International Archives of the Photogrammetry, Remote Sensing and Spatial Information Sciences*, 39:B5, 2012.
- [12] Jiunn-Kai Huang and Jessy W Grizzle. Improvements to target-based 3d lidar to camera calibration. *IEEE Access*, 8:134101–134110, 2020.
- [13] Vincent Fremont, Philippe Bonniaf, et al. Extrinsic calibration between a multi-layer lidar and a camera. In *2008 IEEE International Conference on Multisensor Fusion and Integration for Intelligent Systems*, pages 214–219. IEEE, 2008.
- [14] Lipu Zhou, Zimo Li, and Michael Kaess. Automatic extrinsic calibration of a camera and a 3d lidar using line and plane correspondences. In *2018 IEEE/RSJ International Conference on Intelligent Robots and Systems (IROS)*, pages 5562–5569. IEEE, 2018.
- [15] Weimin Wang, Ken Sakurada, and Nobuo Kawaguchi. Reflectance intensity assisted automatic and accurate extrinsic calibration of 3d lidar and panoramic camera using a printed chessboard. *Remote Sensing*, 9(8):851, 2017.
- [16] Davide Scaramuzza, Ahad Harati, and Roland Siegwart. Extrinsic self calibration of a camera and a 3d laser range finder from natural scenes. In *2007 IEEE/RSJ International Conference on Intelligent Robots and Systems*, pages 4164–4169. IEEE, 2007.
- [17] Xiaojin Gong, Ying Lin, and Jilin Liu. 3d lidar-camera extrinsic calibration using an arbitrary trihedron. *Sensors*, 13(2):1902–1918, 2013.
- [18] Gaurav Pandey, James R McBride, Silvio Savarese, and Ryan M Eustice. Automatic extrinsic calibration of vision and lidar by maximizing mutual information. *Journal of Field Robotics*, 32(5):696–722, 2015.
- [19] Bo Fu, Yue Wang, Xiaqing Ding, Yanmei Jiao, Li Tang, and Rong Xiong. Lidar-camera calibration under arbitrary configurations: Observability and methods. *IEEE Transactions on Instrumentation and Measurement*, 69(6):3089–3102, 2019.

- [20] Pablo García-Gómez, Santiago Royo, Noel Rodrigo, and Josep R Casas. Geometric model and calibration method for a solid-state lidar. *Sensors*, 20(10):2898, 2020.
- [21] Jiarong Lin, Xiyuan Liu, and Fu Zhang. A decentralized framework for simultaneous calibration, localization and mapping with multiple lidars. *arXiv preprint arXiv:2007.01483*, 2020.
- [22] Yani Ioannou, Babak Taati, Robin Harrap, and Michael Greenspan. Difference of normals as a multi-scale operator in unorganized point clouds. In *2012 Second International Conference on 3D Imaging, Modeling, Processing, Visualization & Transmission*, pages 501–508. IEEE, 2012.
- [23] Richard H Byrd, Peihuang Lu, Jorge Nocedal, and Ciyou Zhu. A limited memory algorithm for bound constrained optimization. *SIAM Journal on scientific computing*, 16(5):1190–1208, 1995.
- [24] Alexander Duda and Udo Frese. Accurate detection and localization of checkerboard corners for calibration. In *BMVC*, page 126, 2018.
- [25] Jitao Liu, Songmin Dai, and Xiaoqiang Li. Pccn: Point cloud colorization network. In *2019 IEEE International Conference on Image Processing (ICIP)*, pages 3716–3720. IEEE, 2019.
- [26] Kenji Koide and Emanuele Menegatti. General hand–eye calibration based on reprojection error minimization. *IEEE Robotics and Automation Letters*, 4(2):1021–1028, 2019.